J Mater Sci (2007) 42:10023–10031
DOI 10.1007/s10853-007-2002-2

Experimental study of phase equilibria and solidification microstructures of Mg–Ca–Ce alloys combined with thermodynamic modeling

Milan Hampl · Joachim Gröbner · Rainer Schmid-Fetzer

Received: 25 April 2007 / Accepted: 17 July 2007 / Published online: 6 September 2007

Abstract Thermodynamic descriptions of binary Ca–Ce and ternary Mg–Ca–Ce systems were generated using the Calphad method. Complementary experimental study of phase equilibria and solidification microstructures was done using metallography, scanning electron microscope with energy dispersive X-ray microanalysis and differential scanning calorimetry. The microstructures of these Mg-rich alloys formed during slow solidification and the type and sequence of solid phase precipitation compares well with thermodynamic equilibrium and non-equilibrium calculations.

Introduction

Commercial magnesium alloys, like AZ91, AM50 and AM60 offer an excellent combination of mechanical properties, corrosion resistance, and die castability. However, these alloys have poor creep resistance at temperatures above 125 °C, limiting their applications [1]. Better creep behavior may be achieved by well dispersed precipitations in the alloy, like Mg_2Si, Al_2Ca or Al_2RE [2]. An addition of 1% RE (rare earth metal, usually in form of mischmetal) improves the creep resistance, especially if the Al content is less than 4%. The resultant developed AE series shows the highest strength among all commercial Mg alloys. In recent years an alloy (AX51) containing 0.8% Ca was developed which provided similar creep resistance to AE42 and corrosion resistance to AZ91. The higher Ca content, however, deteriorates die castability due to extensive hot cracking and die sticking [1]. To avoid these effects and furthermore minimize high-cost RE additions, new magnesium alloys contain both, Ca and RE, in combination with Sr and Si. Von Buch [3] describes the commercial alloy MRI153 which contains just this combination of alloying elements. The main component of typical mischmetal is Ce, and, thus, the phase relations between Ca, Ce and Mg are of considerable interest for the development of advanced Mg alloys and their processing. These phase equilibria are not known, not to speak about the thermodynamics; it is the purpose of this study to close this knowledge gap, primarily in the Mg-rich corner of the ternary Mg–Ca–Ce system, by experimental and theoretical investigations. It also comprises the microstructures of these alloys formed during slow solidification and the type and sequence of solid phase precipitation.

M. Hampl · J. Gröbner · R. Schmid-Fetzer (✉)
Institute of Metallurgy, Clausthal University of Technology, Robert-Koch-Str. 42, 38678 Clausthal-Zellerfeld, Germany
e-mail: schmid-fetzer@tu-clausthal.de

Experimental data in literature

Binary systems

The Ca–Ce phase diagram suggested by Massalski et al. [4] is based on the experimental work of Zverev [5]. Zverev studied phase equilibria in the Ca–Ce–Cl system but assumed melting temperatures of pure Ca and Ce that are different from commonly accepted values for these elemental components. The revision of the phase diagram in [4] involved adjustment of temperatures to melting points of pure elements by shifting the temperature of monotectic reaction to maintain the same temperature difference to the melting temperature of Ca. In this system, there is a large miscibility gap in liquid phase, no binary

compounds are present and two invariant reactions are reported.

First experimental investigations in the Ce–Mg system were made by Vogel [6]. Later, Vogel and Heumann [7] refined some transition temperatures and compositions using starting materials with higher purity. They performed thermal analysis, X-ray diffraction (XRD) and optical microscopy to determine the phase diagram up to 50 wt.% of Mg. Haughton and Schofield [8] measured Mg-rich alloys using thermal analysis and a phase diagram with experimental points up to 40 wt.% Ce is presented. Wood and Cramer [9] studied alloys in Mg-rich part of phase diagram using differential thermal analysis, metallography and XRD. New phases were revealed to be formed by peritectic reactions: $CeMg_{12}$, Ce_2Mg_{17} and $CeMg_{8.25}$. The proper stoichiometry of the latter phase was later determined to be Ce_5Mg_{41}. Saccone et al. [10] used Smith thermal analysis to revise the Ce- and Mg-rich parts of the phase diagram.

A detailed thermodynamic assessment of the Ce–Mg system is presented by Nayeb-Hashemi and Clark [11] and is mostly based on the work of Vogel [7]. In our work, the thermodynamic description of binary Ce–Mg system is based on the work of Cacciamani et al. [12]. For the Ca–Mg system, the assessment from Agarwal et al. [13] is accepted.

Ternary system

No phase diagram of the ternary Mg–Ca–Ce system could be found in literature. Semenenko and Verbetskiy [14] prepared ten ternary Mg-rich alloys with compositions up to 33 at.% Ca and 11 at.% Ce by melting under flux. XRD of as-cast alloys showed two binary phases $CaMg_2$ and $CeMg_{12}$ together with (Mg) phase. His main focus was on the measurement of hydrogen solubility in these alloys.

Experimental investigation

The present experimental investigation of Mg–Ca–Ce phase equilibria was carried out using scanning electron microscopy (SEM) with energy dispersive X-ray microanalysis (SEM/EDX) and differential scanning calorimetry (DSC).

Eight samples with different compositions, selected by preliminary thermodynamic calculations to be most relevant, were prepared from high purity metals. Starting materials were magnesium chips (99.98 mass%, Alfa), Ca granules (99.5 mass%, Alfa, Karlsruhe, Germany) and Ce bulk (99.9 mass%, Auer-Remy, Hamburg, Germany). All samples were sealed under argon atmosphere by welding in customized thin-walled tantalum capsules to avoid evaporation and oxidation. Typical sample weight was about 200 mg. Reaction temperatures were measured by DSC in a heat-flux cylindrical Calvet-type calorimetric system Multi HTC 96 (Setaram, Caluire, France). The equipment was calibrated using pure metals, Ag, Al, Au, In, Pb and Sn. Sapphire sealed in a duplicate tantalum capsule was used as reference material. Before measurement the analysis chamber was evacuated and then helium was applied as a flowing gas in the analysis chamber with a flow rate of 2 L/min. The DSC measurements were carried out with heating/cooling rates of 5 and 1 K/min and multiple heat cycling to ensure reproducibility.

Solidification microstructures and phase compositions were studied by SEM using mainly back-scattered electrons (BSE) and SEM/EDX. After the last DSC cooling cycle with 1 K/min samples were removed quickly from the Ta-capsule and polished under alcohol to avoid reaction with water. Etching was not necessary. Immediately after polishing they were studied by SEM/EDX. XRD of the samples was not carried out due to the rapid oxidation of calcium compounds in the air.

Thermodynamic calculation

Binary system Ca–Ce

The Gibbs energy function $G_i^{0,\phi}(T) = G_i^{\phi}(T) - H_i^{\mathrm{SER}}$ for the element i (i = Ca, Ce) in the ϕ phase (ϕ = fcc (αCa, αCe), bcc (βCa, βCe) or liquid) is described by the equation:

$$G_i^{0,\phi}(T) = a + b\cdot T + c\cdot T\ln T + d\cdot T^2 + e\cdot T^3 + f\cdot T^{-1} + g\cdot T^7 + h\cdot T^{-9} \quad (1)$$

where H_i^{SER} is the molar enthalpy for the stable element reference (SER) at 298.15 K and 1 bar, and T is the absolute temperature. The Gibbs energy functions for Ca and Ce are taken from the SGTE compilation by Dinsdale [15].

The liquid, fcc (αCa, αCe) and bcc(βCa, βCe) solution phases are described by the substitutional solution model. For the liquid phase the molar Gibbs energy is expressed by following equation:

$$G^{\mathrm{Liq}} = (1-\mathrm{x})G_{\mathrm{Ca}}^{0,\mathrm{Liq}} + \mathrm{x}\,G_{\mathrm{Ce}}^{0,\mathrm{Liq}} + \mathrm{RT}[\mathrm{x}\ln\mathrm{x} + (1-\mathrm{x})\ln(1-\mathrm{x})] + L_{\mathrm{Ca,Ce}}^{0,\mathrm{Liq}}\mathrm{x}(1-\mathrm{x}) \quad (2)$$

in which R is the gas constant, and x is the molar fraction of Ce. The interaction parameter $L_{\mathrm{Ca,Ce}}^{0,\mathrm{Liq}}$ was optimized to be 38 kJ/mol. The phases fcc (αCa, αCe) and bcc(βCa, βCe) are described by analogous equations for a regular solution

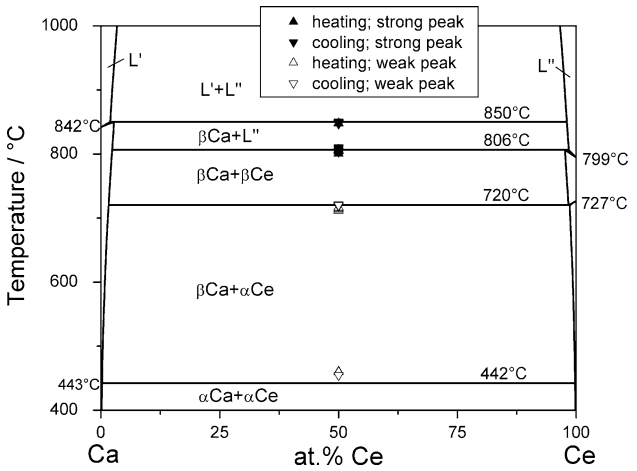

Fig. 1 Calculated binary phase diagram of the binary Ca–Ce system with present experimental data (sample no. 8)

with interaction parameters $L^{0,fcc}_{Ca,Ce} = 36\,kJ/mol$ and $L^{0,bcc}_{Ca,Ce} = 35\,kJ/mol$ respectively. The calculated phase diagram compared with our experimental data is shown in Fig. 1.

Ternary system Mg–Ca–Ce

The ternary system was calculated using the unary data for Mg [15] and the binary data for Ca–Mg [13] and Ce–Mg [12], together with the present data set for Ca–Ce as described above. Experimentally observed solubility of Ca in the compound Ce_5Mg_{41} was modeled by a simple substitutional solution model represented by formula $(Ca,Ce)_5Mg_{41}$. The Gibbs energy (per mol of atoms) is expressed by

$$\begin{aligned} G^{(Ca,Ce)_5Mg_{41}} &= y_{Ca}G^{0,Ca_5Mg_{41}}_{Ca:Mg} + y_{Ce}G^{0,Ce_5Mg_{41}}_{Ce:Mg} \\ &+ \frac{5}{46}RT(y_{Ca}\ln y_{Ca} + y_{Ce}\ln y_{Ce}) \\ &+ y_{Ca}y_{Ce}(y_{Ca} - y_{Ce})L^{1,(Ca,Ce)_5Mg_{41}}_{Ca,Ce:Mg} \end{aligned} \quad (3)$$

in which y_{Ca} and y_{Ce} are the site fractions of Ca and Ce on the first sublattice. The parameters $G^{0,\phi}_{*:Mg}$ are expressed relative to the Gibbs energies of the pure elements at the same temperature. The quantity $G^{0,Ce_5Mg_{41}}_{Ce:Mg}$ is taken from binary description of the Ce–Mg system and the parameter $G^{0,Ca_5Mg_{41}}_{Ca:Mg} = (-250 + 0.3T)/46\,kJ(mol\ of\ atoms)^{-1}$ was set large enough to make the end member $(Ca)_5Mg_{41}$ unstable in the binary Ca–Mg system because no binary phase with this stoichiometry is present. The L parameter represents interaction primarily within the sublattice. Just one constant interaction parameter $L^{1,(Ca,Ce)_5Mg_{41}}_{Ca,Ce:Mg} = +220/46\,kJ(mol\ of\ atoms)^{-1}$ with no temperature dependence was used to fit the experimentally found maximum solid solubility of 1.1 at.% Ca in the $(Ca,Ce)_5Mg_{41}$ phase, using its liquidus temperature as an additional check.

No ternary parameter was necessary in the description of the liquid phase using a standard Redlich-Kister-Muggianu type extrapolation. For all calculations, the software package PANDAT [16] was used.

Results

Table 1 shows the sample compositions and phases observed in the microstructures by SEM/EDX. Primary crystallizing phases, denoted by bold font, were identified from their morphology in the solidification microstructure. No ternary phases were observed in this system. Sample compositions were focused to check all invariant reactions in the Mg-rich corner. Thus, no ternary alloys were prepared within the large miscibility gap originating from the Ca–Ce binary. One sample, no. 8, was sufficient to check all the pertinent invariant equilibria in the Ca–Ce binary because of the strong demixing in all solid and liquid phases.

The results of DSC measurements and their interpretation are summarized in Table 2. For the cooling curves, onset temperatures are determined. The heating peaks are interpreted according to the peak shape analysis; for invariant reactions, onset temperatures are determined and otherwise peak maximum temperatures are evaluated. Some signals were weak and diffuse as indicated. The entries in the column "Interpretation" are in accord with the phase boundaries or invariant reactions calculated for the specific alloy, unless indicated by question mark.

In Fig. 1, the calculated binary phase diagram of the system Ca–Ce is presented. The binodal temperature was not measured because of temperature limitations of our DSC equipment. Observation of microstructure of sample no. 8 confirmed the presence of two pure metals, Ca and Ce, respectively, in agreement with phase diagram in Fig. 1. Calculated temperatures of invariant reactions in binary Ca–Ce system are compared to measured data in Table 3. It is noted that the invariant temperatures are key features, determining the entire binary equilibria in any reasonable modeling.

The calculated ternary liquidus surface is shown in the Fig. 2. The large liquid miscibility gap dominates the Mg-poor alloys. Calculated invariant reactions in the ternary Mg–Ca–Ce system, corresponding to Fig. 2 and compared with present experimental data, are shown in Table 4. For example, U_1 denotes the reaction in Table 4, whereas U_1' and U_1'' denote the corresponding liquid compositions in Fig. 2. The reaction U_2 at 615 °C is virtually degenerate, because all three solid phases belong to the Ce–Mg binary system and no consumption of the ternary liquid L occurs.

Table 1 Sample compositions and phase assembly derived from SEM/EDX analysis in this work

Sample no.	Sample composition/at.%			Phases identified by SEM/EDX
	Ca	Ce	Mg	
1	2.3	1.0	96.7	**(Mg)** + $CeMg_{12}$
2	4.0	3.0	93.0	**$CeMg_{12}$** + (Mg)
3	3.0	4.0	93.0	**$CeMg_{12}$** + (Mg)
4	5.7	6.3	88.0	**Ce_5Mg_{41}** + $CaMg_2$ + (Mg)
5	8.2	8.2	83.6	**$CeMg_3$** + Ce_5Mg_{41} + $CaMg_2$
6	25.0	4.0	71.0	**$CaMg_2$** + $CeMg_{12}$
7	15.0	22.0	63.0	**$CeMg_3$** + CeMg
8	50.0	50.0	–	(Ca) + (Ce)

Bold font denotes primary crystallizing phases

Table 2 Temperatures extracted from the DSC curves obtained by thermal analysis in the Mg–Ca–Ce system and their interpretation

Sample no.	Thermal signal		Interpretation
	Heating[a]/°C	Cooling[b]/°C	
1	514 s	512 s	E_2
	555 w	552 w	L + (Mg)/L + (Mg) + $CeMg_{12}$
	611 w	611 w	L/L + (Mg)
	646 w	643 w	?
2	512 s	514 s	E_2
	550 w	552 w	L + $CeMg_{12}$/L + $CeMg_{12}$ + (Mg)
	561 w	564 w	L/L + $CeMg_{12}$
3	514 w	514 w	E_2
	569 s	566 s	L + $CeMg_{12}$/L + $CeMg_{12}$ + (Mg)
	587 s	586 s	L/L + $CeMg_{12}$
4	513 s	512 s	E_2
	539 w	541 w	U_6
	607 w	592 w	L/L + Ce_5Mg_{41}
5	513 s	512 s	E_2?
	575 s	592 s	U_5
	607 w	608 w	?
	640 w	646 w	L/L + $CeMg_3$
6	511 s	516 s	E_2?
	534 w	–	?
	564 w	551 w	?
	737 s	740 s	L/L + $CaMg_2$
7	663 w	664 w	?
	769 s	768 s	L/L + $CeMg_3$?
8	459 w	454 w	βCa = αCa (($+\alpha$Ce))
	715 w	720 w	βCe = αCe + βCa
	805 s	805 s	L′′ + βCa = βCe
	848 s	849 s	L′ + L′′ = βCa

[a] Onset for invariant reaction, maximum otherwise

[b] Onset

s—strong and clear signal

w—weak and diffuse signal

?—correlation to calculated equilibria unclear

The seemingly similar reaction U_4 at 611 °C is not degenerate, even though the liquid contains only 0.02 at.% Ca. This is because the phase Ce_5Mg_{41} has ternary solubility and, thus, U_4 is a true transition-type reaction, occurring in fact 2 K above the related binary eutectoid decomposition of Ce_2Mg_{17} at 609 °C.

A detailed representation of the liquidus surface in the Mg-rich corner with monovariant reaction lines and isotherms is shown in Fig. 3. This Mg-rich part, which is in the focus of our interest, exhibits two large primary solidification fields, $CeMg_3$ and $CaMg_2$, and three smaller fields, Ce_5Mg_{41}, $CeMg_{12}$ and (Mg) are present. The

Table 3 Binary Ca–Ce invariant reactions from thermodynamic calculations compared with present experimental data

Invariant reaction	Temperature/°C	
	Calc.	Exp.
$L' + L'' = \beta Ca$	850	849
$L'' + \beta Ca = \beta Ce$	806	805
$\beta Ce = \alpha Ce + \beta Ca$	720	720
$\beta Ca = \alpha Ca (+\alpha Ce)$	442	454

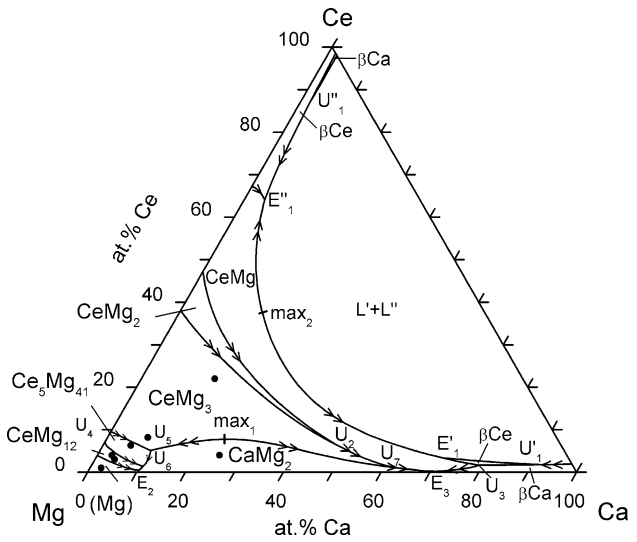

Fig. 2 Calculated Mg–Ca–Ce liquidus surface. Dots represent sample compositions

primary field of Ce_2Mg_{17} is so small that it cannot be detected on a graph, thus the associated reaction U_4 occurs almost at the binary Mg–Ce edge with a liquid composition

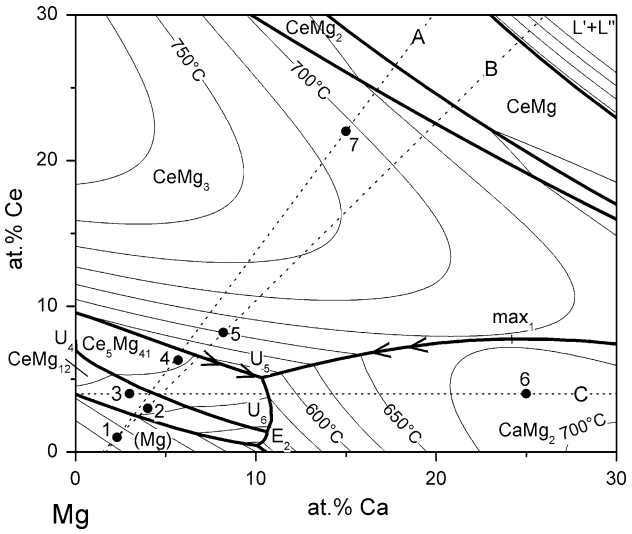

Fig. 3 Calculated Mg–Ca–Ce liquidus surface of Mg-rich corner. Numbered dots represent investigated sample compositions; dotted lines labeled A, B and C indicate directions of calculated vertical sections presented later. Monovariant reaction lines are shown as thick lines and isotherms as thin lines with steps of 25 °C

of 0.02 at.% Ca and 7 at.% Ce. All seven ternary samples, represented by numbered dots, are located in the area of Fig. 3 to study all relevant primary crystallizing phases and subsequent solidification reactions and microstructures. The dotted lines, *A*, *B* and *C*, represent the directions of calculated vertical phase diagram sections, which are presented in Figs. 4–6. Three invariant reactions were experimentally observed in the composition range of Fig. 3, specifically two transition reactions, U_5 and U_6, and one ternary eutectic E_2. The observed solidification microstructures will be presented in the following section.

Table 4 Calculated invariant reactions in the ternary Mg–Ca–Ce system involving the liquid phase, compared with present experimental data

Type	Invariant reaction	Temperature/°C	
		Calc.	Exp.
U_1	$L'' + \beta Ca = L' + \beta Ce$	775	–
max_1	$L' = CaMg_2 + CeMg_3$	672	–
max_2	$L' + L'' = CeMg$	670	–
E_1	$L'' = \beta Ce + CeMg + L'$	653	–
U_2	$L + CeMg_2 = CeMg + CeMg_3$	615	–
U_3	$L + \beta Ce = CeMg + \beta Ca$	612	–
U_4	$L + Ce_2Mg_{17} = Ce_5Mg_{41} + CeMg_{12}$	611	–
U_5	$L + CeMg_3 = CaMg_2 + Ce_5Mg_{41}$	582	591
U_6	$L + Ce_5Mg_{41} = CaMg_2 + CeMg_{12}$	542	540
U_7	$L + CeMg_3 = CeMg + CaMg_2$	532	–
E_2	$L = CeMg_{12} + CaMg_2 + (Mg)$	514	513
E_3	$L = \beta Ca + CaMg_2 + CeMg$	445	–

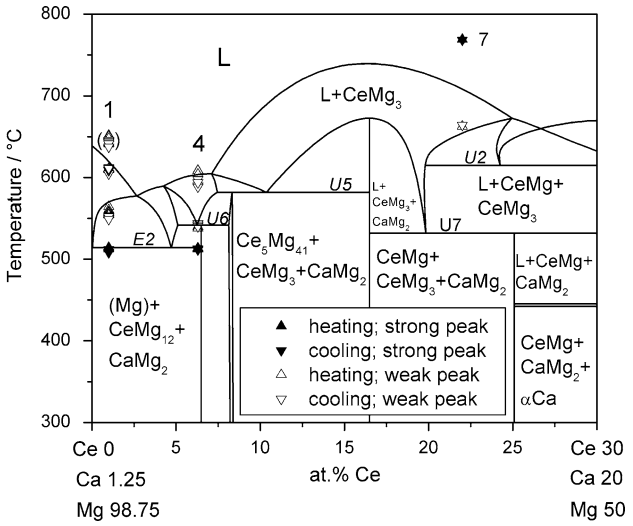

Fig. 4 Calculated vertical section *A* including the DSC signals from samples 1, 4 and 7

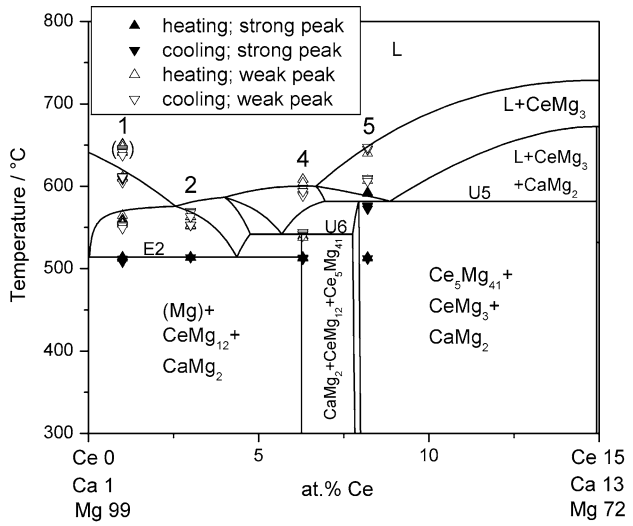

Fig. 5 Calculated vertical section *B* including the DSC signals from samples 1, 2, 4 and 5

Discussion

The Binary Ca–Ce system

Temperatures of four invariant reactions in the binary system were determined by DSC technique and the thermodynamic parameters of solution phases were optimized according to these temperatures, resulting in a good overall agreement. Solubilities of Ca in αCe and βCe and of Ce in αCa and βCa are compulsory since the measured invariant temperatures are clearly above the melting points of the pure components. These solubilities have not been directly measured, though, since such details were out of the scope

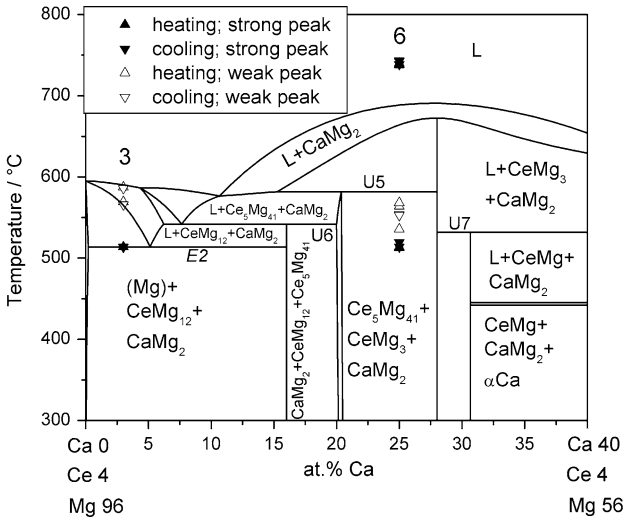

Fig. 6 Calculated vertical section *C*, at constant 4 at.% Ce, including the DSC signals from samples 3 and 6

of the present investigation. Zverev [5] had reported the temperatures of two invariant reactions, at 843 and 802 °C, respectively. We measured these invariant reactions at 849 and at 805 °C and both values are in a good agreement with the presently calculated values as shown in Table 3 and Fig. 1. It is noted that the invariant reaction at 850 °C is not a monotectic but a syntectic one, due to the solid solubility. This is proven by the fact that the measured invariant temperature is 8 K above the melting point of Ca, whereas for a monotectic reaction it should be below 842 °C.

Solidification of ternary Mg–Ca–Ce alloys

Both the thermal analysis data and the experimentally observed microstructures of the samples after slow solidification in the DSC have to be addressed jointly. For this purpose we will use in the following our calculated phase diagrams, and also thermodynamic calculations under equilibrium and non-equilibrium Scheil conditions [17] for selected alloys, each showing a different primary crystallization. The sequence of phase formation resulting from this analysis is found to support the thermodynamic description for all the alloys studied. For the Mg-poorest samples no. 6 and 7 the agreement is restricted to the primary phases.

The calculated vertical section *A* is compared in Fig. 4 with DSC data of samples no. 1, 4 and 7. The DSC signals from alloys 1 and 4 are in a good agreement with calculated phase transitions, except the highest signals of sample 1; these weak signals are bracketed since their experimental evidence is not clear. They might correspond with

the melting temperature from some unreacted, isolated Mg. The liquidus temperature of the Mg-poorest sample 7 was determined at much higher temperature than calculated and no signal was detected at the invariant reactions U_2 and U_7. Figure 7 shows an electron micrograph of sample no. 1, displaying the mass contrast of phases with BSE. Primary crystallizing solid solution of (Mg) is seen, the bright secondary phase $CeMg_{12}$ and in the final tertiary solidification step the fine eutectic matrix. This eutectic matrix, corresponding to reaction E_2 at 514 °C, consists mainly of (Mg) and $CaMg_2$ with a small amount of $CeMg_{12}$ and a calculated overall composition of 10 at.% Ca and 0.45 at.% Ce. This is in qualitative agreement with the EDX analysis of representative areas of this matrix, also found in samples 2, 3 and 4; the primary and secondary phases are also identified subject to the typical accuracy of the EDX analysis. The calculated phase formation for this alloy is virtually the same for Scheil and equilibrium modes of solidification because only decomposition-type reactions and negligible solid solubilities are involved. Both calculations agree well with the observed microstructure.

The microstructure of sample no. 4, also located on section *A*, is presented in Fig. 8. Here Ce_5Mg_{41} is detected as primary crystallizing phase; the secondary $CaMg_2$ is surrounded by a fine eutectic matrix. The large blocks of Ce_5Mg_{41} allow a better EDX analysis; a solubility of 1.1 at.% Ca is measured in this phase, which is double the value observed in any of the other Ce–Mg binary intermetallics in all samples. This is the reason why only Ce_5Mg_{41} is modeled with a corresponding solubility of Ca. The primary and secondary solidification are again supported by the Scheil and equilibrium calculations, which do not differ until the tertiary step, where the reaction U_6 at 542 °C is encountered. Under equilibrium conditions the entire amount of Ce_5Mg_{41} (60%) should be completely consumed for this alloy in the transition-type reaction U_6, $L + Ce_5Mg_{41} = CaMg_2 + CeMg_{12}$. Under Scheil conditions a solid phase cannot be consumed; all of the Ce_5Mg_{41} is frozen-in and solidification proceeds along the monovariant eutectic $L = CaMg_2 + CeMg_{12}$ until the ternary eutectic E_2 at 514 °C is reached with a large amount (30%) of residual liquid, 10 times more than in the equilibrium case. It is obvious from Fig. 8 that the sample followed more closely the Scheil mode, despite the slow solidification rate of only 1 K/min. This is also supported by the thermal signals, which are only weak at U_6 and very strong at E_2.

The vertical section *B* is presented in Fig. 5. Signals from sample no. 1, located roughly on both sections *A* and *B*, have been discussed above. The liquidus temperature of sample no. 2 is lower than the calculated one, but the eutectic temperature E_2 agrees well with the calculation. Both invariant reactions U_6 and E_2 and the liquidus temperature of sample no. 4 agree very well with the phase diagram. Sample no. 5 shows DSC signals for the transition-type reaction U_5, but also for the ternary eutectic reaction E_2 that should not occur in equilibrium for this alloy composition. This is explained by an unfinished transition-type reaction U_5. An electron micrograph of sample no. 5 is shown in Fig. 9. $CeMg_3$ crystallizes as a primary phase, the secondary phase is Ce_5Mg_{41}. So far the Scheil and equilibrium calculations for this alloy are essentially the same until reaction U_5 at 582 °C is reached.

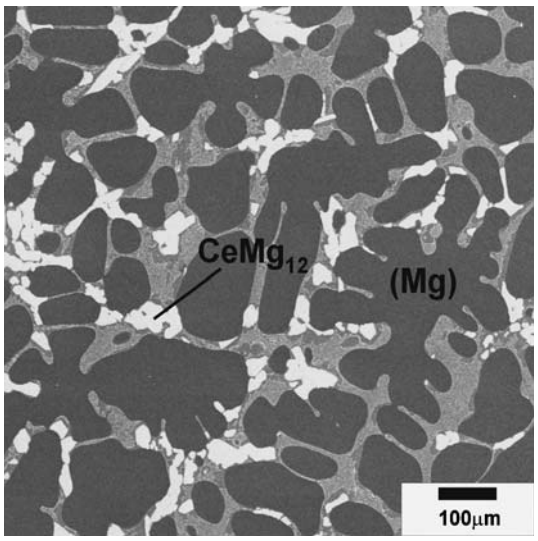

Fig. 7 Electron micrograph (BSE) of the sample 1 (Ca2.3 Ce1.0 Mg96.7) showing primary phase (Mg), secondary phase $CeMg_{12}$ and eutectic matrix

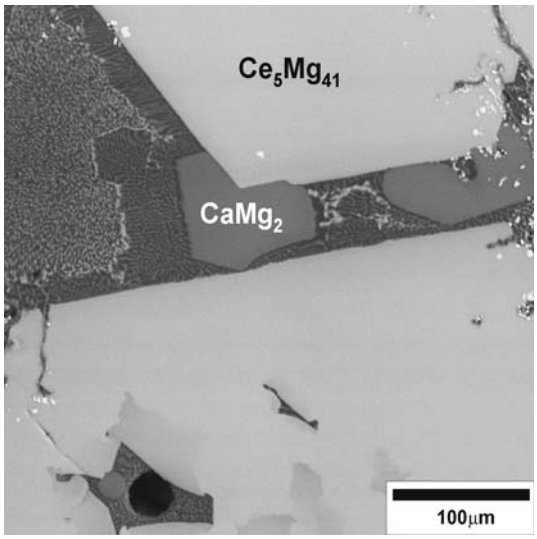

Fig. 8 Electron micrograph (BSE) of the sample 4 (Ca5.7 Ce6.3 Mg88.0) showing primary phase Ce_5Mg_{41} and secondary phase $CaMg_2$. White particles are residues from tantalum capsule introduced from metallographic preparation

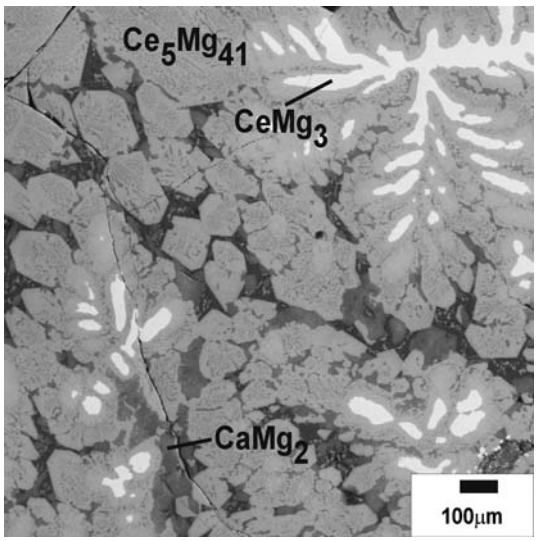

Fig. 9 Electron micrograph (BSE) of the sample 5 (Ca8.2 Ce8.2 Mg83.6) showing primary phase $CeMg_3$ and secondary phase Ce_5Mg_{41}. The phase $CaMg_2$ precipitates subsequently in reaction U_5

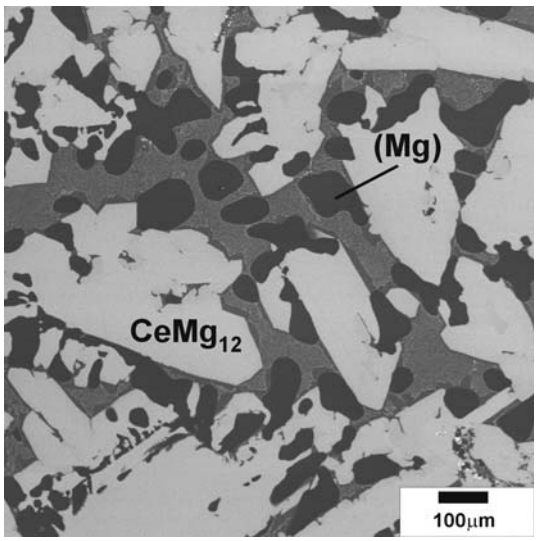

Fig. 10 Electron micrograph (BSE) of the sample 3 (Ca3.0 Ce4.0 Mg93.0) showing primary phase $CeMg_{12}$, secondary phase (Mg) and eutectic matrix

If equilibrium prevails the solidification should terminate by a complete consumption of liquid according to the reaction L + $CeMg_3$ = $CaMg_2$ + Ce_5Mg_{41}, with only 3% of $CeMg_3$ phase left. By contrast, under Scheil conditions the 14% of $CeMg_3$ phase are frozen-in and the residual liquid proceeds along the monovariant L = $CaMg_2$ + Ce_5Mg_{41}, passing U_6 at 542 °C and terminating at the ternary eutectic E_2. This corresponds much closer to the observed microstructure and also to the observed non-equilibrium thermal signal at E_2.

In Fig. 6, DSC signals from samples no. 3 and 6 are compared with the calculated vertical section at constant 4 at. % Ce. Sample no. 3 corresponds very well with calculated equilibrium phase boundaries. This is compounded by the fact that the calculated phase amounts during solidification virtually agree under Scheil and equilibrium conditions and are also reflected in the microstructure of sample no. 3 given in Fig. 10. Primary crystallization of $CeMg_{12}$ is followed by the secondary monovariant L = $CeMg_{12}$ + (Mg), ending in the tertiary step in the ternary eutectic E_2. The measured liquidus temperature of the Mg-poor sample no. 6 in Fig. 6 is about 60 K higher than calculated. This sample also exhibits the thermal signals of a non-equilibrium solidification path by continuing beyond the transition reaction U_5, passing U_6 and terminating at E_2.

Ternary Mg–Ca–Ce phase equilibria

The calculated solid state phase equilibria are presented in an isothermal section of the Mg–Ca–Ce system at 400 °C

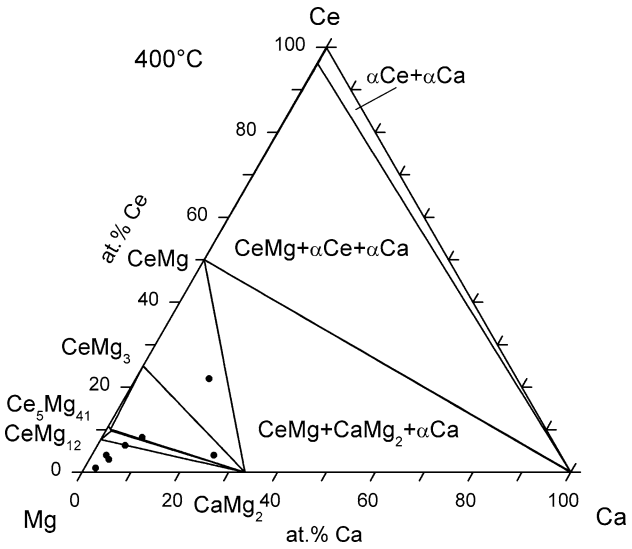

Fig. 11 Calculated isothermal section at 400 °C, showing the solid state phase equilibria. Dots represent sample compositions

in Fig. 11. Compositions of the present samples are superimposed. Only two phases exhibit a noticeable solubility range: αCe dissolves some Mg, and Ce_5Mg_{41} dissolves some Ca. In the Mg-rich corner the (Mg) solid solution with only 0.2 at.% Ca and negligibly dissolved Ce is in equilibrium with the two stoichiometric phases $CeMg_{12}$ and $CaMg_2$.

Figure 12 shows the comparison between the measured and calculated liquidus and eutectic temperatures, respectively. The calculated data are generated from the thermodynamic calculation using the exact compositions of all seven ternary alloy samples. This allows a

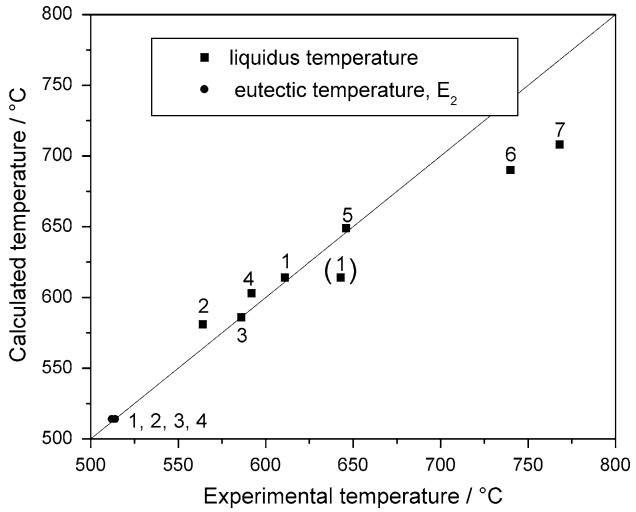

Fig. 12 Comparison between experimentally observed thermal signals and results from thermodynamic calculations for all ternary alloy samples

comprehensive comparison irrespective of the location of samples on the vertical composition sections.

The experimental values of liquidus temperatures are in good agreement for alloys no. 1–5, however, for the two Mg-poorest samples no. 6 and 7 the difference is large. For these high alloyed samples the influence of ternary interactions in the liquid phase may be appreciable and the calculation without the use of ternary parameters might be not appropriate. It was decided not to sacrifice the simple and robust thermodynamic description of this ternary system for a better fitting of these data which are in a marginal area. The measured temperature of the ternary reaction E_2 is in excellent agreement with calculation, the difference is within 2 °C for alloys no. 1–4.

This agreement is also seen in the comparison of calculated and experimental invariant reaction temperatures in Table 4. Reactions E_2 and U_6 correspond very well with calculated values, whereas reaction U_5 exhibits a larger difference. The other invariant reactions, outside of the Mg-rich corner, are compiled in order to present a complete and internally consistent phase diagram of the entire system as given by the thermodynamic extrapolation calculation from the binary edge systems.

Conclusion

A thermodynamic assessment was worked out parallel to experimental study in Ca–Ce binary and Mg–Ca–Ce ternary systems. All experimental data are well described by the calculated ternary phase diagram for samples with more than 71 at.% Mg. Only a small solid solubility of Ca in Ce_5Mg_{41} was observed, but no ternary solid phases.

The calculated liquidus surface of all primary crystallizing phases in the Mg-rich corner is reproduced properly and solidification sequences are in an excellent agreement with observed micrographs. These solidification microstructures are also elucidated using thermodynamic equilibrium and non-equilibrium (Scheil-type) calculations for individual alloys. Depending on the reaction type in the phase diagram the solidification may follow more closely the non-equilibrium path even for cooling rates as low as 1 K/min.

The Mg-poor part of the ternary system, not in the focus of this study, is presented based on the thermodynamic extrapolation calculation from the edge binaries; it is only qualitatively supported by the samples with 63 and 71 at.% Mg. At lower Mg-content the large liquid miscibility gap, originating from the Ca–Ce binary edge, is expected to occur up to 47 at.% Mg. Its quantitative extension into the ternary is not verified.

Acknowledgement This study is supported by the German Research Foundation (DFG) in the Priority Programme "DFG-SPP 1168: InnoMagTec" under grant no. Schm 588/26.

References

1. Luo AA (2004) Int Mater Rev 49:13
2. Pekguleryuz MO, Kaya AA (2003) Adv Eng Mater 5(12):866
3. Buch FV, Schummann S, Friedrich H, Aghion E, Bronfin B (2002) Metall 56:40
4. Massalski TB, Okamoto H, Subramanian PR, Kacprzak L (eds) (1990) In: Binary alloy phase diagrams, 2nd edn, Vols. 1–3, 3589 pp. ASM International, Materials Park, OH 44073, p 902
5. Zverev GL (1955) Dokl Akad Nauk SSSR 104:242
6. Vogel R (1915) Z Anorg Allg Chem 91:277
7. Vogel R, Heumann T (1947) Z Metallkde 38:1
8. Haughton JL, Schofield TH (1936) J Inst Met 60:339
9. Wood DH, Cramer EM (1965) J Less-common Met 9:321
10. Saccone A, Maccio D, Delfino S, Hayes FH, Ferro R (2001) J Therm Anal Calorim 66:47
11. Nayeb-Hashemi AA, Clark JB (1988) Bull Alloy Phase Diagrams 9(2):78
12. Cacciamani G, Borzone G, Ferro R (1998) In: COST507—Thermochemical Database for Light Metal Alloys. European Commission EUR 18499 EN, pp 137–140
13. Agarwal R, Lee JJ, Lukas H-L, Sommer F (1995) Z Metallkd 86:103
14. Semenenko KN, Verbetskiy VN (1984) Vestn Mosk Univ Ser 2 Khim 25(5):509
15. Dinsdale AT (1991) CALPHAD 15:317
16. Chen S-L, Daniel S, Zhang F, Chang YA, Yan X-Y, Xie F-Y, Schmid-Fetzer R, Oates WA (2002) CALPHAD 26:175
17. Scheil E (1942) Z Metallkde 34:70